

A-Bing Lin, Sonja Aulbach, Jian-Ping Zheng, Ronghua Cai, Jingao Liu, Qing Xiong, and Shao-Kui Pan, 2022, Lithospheric mantle provinces and crust-mantle decoupling beneath northeastern China: Insights from peridotite xenoliths: GSA Bulletin, <https://doi.org/10.1130/B36338.1>.

Supplemental Material

Supplementary Information 1. Geological and geodynamic setting

Supplementary Information 2. Petrography

Supplementary Information 3. Analytical methods

Figure S1. Field photographs and photomicrographs.

Figure S2. Backscattered electron image and elemental maps.

Figure S3. Trace-element patterns.

Figure S4. BSE images and elemental maps of sulfide grains.

Figure S5. Olivine mode and FeO in whole rocks.

Figure S6. Calculated melts in equilibrium with clinopyroxene.

Table S1. Major-element compositions of whole rocks.

Table S2. Major-element compositions of minerals.

Table S3. Trace-element compositions of clinopyroxene.

Table S4. Sr isotopic compositions of clinopyroxene.

Table S5. Temperature and oxygen fugacity.

Table S6. Mineral modes and reconstructed whole-rock compositions.

Table S7. Distribution coefficients.

SUPPLEMENTARY INFORMATION 1. **GEOLOGICAL AND GEODYNAMIC SETTING**

The eastern part of the Central Asian Orogenic Belt (CAOB) in northeastern China (NEC) was formed by the subduction and amalgamation of several micro-continents during the Proterozoic through the Paleozoic (Fig. 1; Jahn et al., 2000). The tectonic evolution of this region during the Mesozoic includes the final closure of the Paleo-Asian Ocean in the south and overprinting effects of the circum-Pacific and Mongol-Okhotsk tectonic systems in the east and north, respectively (Li, 2006; Xu et al., 2013). Complex mantle dynamics, involving downwelling beneath the southern Songliao basin and upwelling beneath various volcanoes (Changbaishan, Jingpohu, Halaha and Abaga) in the northeastern NCC and NEC (Fig. 1B), have been linked to anomalously low S-wave velocity in the upper mantle (Tang et al., 2014; Guo et

al., 2016, 2018). During the Cenozoic, this region experienced intense and widespread basaltic activity (Fig. 1B). The Cenozoic volcanism in NEC, distributed along the western Pacific margin, occurs ~1300 km from the Japanese Trench, distinct from those occurring at plate boundaries (Liu et al., 2001). This intraplate volcanism has been attributed to the upwelling of hot and wet asthenospheric material (Lei and Zhao, 2005) or of hot and buoyant sublithospheric mantle (Tang et al., 2014), in both cases related to the Pacific Plate that is now stalled in the mantle transition zone (Lei and Zhao, 2005; Tang et al., 2014), in addition to melting related to on-going passive lithospheric upper mantle convection (Guo et al., 2018).

Cenozoic volcanism in NEC is dominated by alkali and highly potassic basalts with subordinate tholeiites, and abundant mantle xenoliths were reported from several volcanic fields (e.g., Pan et al., 2013, 2015; Zhang et al., 2011, 2012, 2019). Among them, the Jiaohe volcanic field in central Jilin Province, part of Jingpohu volcano, erupted during the late Cenozoic (5.05–2.75 Ma, Wang, 1996). Jiaohe basalts are mainly composed of basanites, alkaline olivine basalts and corresponding pyroclastic rocks, which unconformably cover the Paleozoic strata and Mesozoic granites, and the exposed thickness is more than 56 m (Zhou et al., 2007). Volcanic activity in the Jiaohe area was controlled by the Dunhua-Mishan fault (DMF), which together with the Yilan-Yitong fault (YYF) constitute the two branches of the trans-lithospheric Tan-Lu fault belt (TLFB) in NEC (Fig. 1B). Both branches record Early Cretaceous activity, ascribed to the subduction of the Izanagi and Pacific plates, with a 35 km and 170 km sinistral displacement along the YYF and the DMF, respectively, and a total northward offset of ~205 km in NEC (Liu et al., 2019).

The xenoliths entrained by the Jiaohe alkali basalts consist of spinel peridotites and garnet-bearing pyroxenites (Zhou et al., 2007; Yu et al., 2009, 2010), which were collected from a quarry at Yiqisong. The $^{187}\text{Os}/^{188}\text{Os}$ ratios of 0.1178–0.1396 reported for 10 peridotites from this location (Zhou et al., 2007) show that the two most refractory harzburgites ($\text{Al}_2\text{O}_3 < 2$ wt%) have Re depletion ages (T_{RD}) of 1.1 and 1.6 Ga, respectively. The peridotites from the same site show that some of them have decoupled Nd–Hf isotope ratios, which is attributed to pervasive mantle metasomatism by an asthenosphere-derived silicate melt (Yu et al., 2009). In addition, Guo et al. (2020) suggest that Jiaohe peridotite and pyroxenite xenoliths were metasomatized by melts originated from carbonated asthenosphere. The whole-rock H_2O contents of 4 Jiaohe peridotites vary from 10 to 116 ppm, similar to those of xenoliths from the NCC, but different from the completely dry lithospheric mantle beneath the northern part of NEC, such as Nuomin (Hao et al., 2016). The olivine grains in some xenoliths have gem quality, while related olivine mines in Jiaohe are mainly at Dashihe and Yiqisong. A suite of spinel-facies peridotite xenoliths were collected from Dashihe for the present study, including 16 lherzolites and 4 harzburgites (Fig. 2).

The Longgang volcanic field in the northeastern corner of the NCC (i.e., Huinan; Fig. 1) is composed of more than one hundred cinder cones, many of which were erupted in the early Pleistocene (0.6 Ma; Xu et al., 2003). These Cenozoic alkali basalts entrained abundant mantle-derived megacrysts and xenoliths. Re-Os isotopic compositions of 11 peridotites from three localities (Dayishan, Dalongwan and Longquanlongwan) reported by Wu et al. (2003) show $^{187}\text{Os}/^{188}\text{Os}$ ratios of 0.1186–0.1289, with T_{RD} of 0.7–1.5 Ga for 7 refractory samples ($\text{Al}_2\text{O}_3 < 2$ wt%). Xu et al. (2003) suggest that the harzburgites from Huinan are not simple residues of partial melting, but likely transformed from lherzolites by melt-rock interaction.

The relatively refractory peridotites from Huinan have ubiquitous spinel-pyroxene intergrowths indicative of garnet destabilization, which is ascribed to reaction at low melt-rock

ratios, whereas the absence of such intergrowths in fertile peridotites resulted from melt-rock interaction at high melt–rock ratios (Lin et al., 2019). Six relatively refractory peridotites collected from Dayishan studied by Lin et al. (2019) are further used for PGE and Re-Os isotope analyses in this study.

SUPPLEMENTARY INFORMATION 2. PETROGRAPHY

Peridotite xenoliths from the Jiaohé volcanic field are abundant, fresh, rounded or ellipsoidal and relatively large, with diameters ranging mostly between 5 and 10 cm (Fig. S1A–B). All peridotites consist of olivine, orthopyroxene (Opx), clinopyroxene (Cpx) and spinel, and lack volatile-bearing accessory minerals, such as apatite, amphibole, phlogopite and carbonate. They have coarse-grained protogranular (Fig. S1C–D) to “porphyroclastic” textures based on grain size distribution (Fig. S1E), and contain well-developed triple junctions among mineral grains of nearly all samples (Fig. S1C). For the protogranular peridotites, olivine and Opx generally occur as large crystals ranging between 2 and 5 mm and often displaying curvilinear to rectilinear grain boundaries. Clinopyroxene and spinel are ~0.5–1.5 mm in size and commonly occur as anhedral grains interstitial phases at grain boundaries of peridotite mineral constituents. Compared to the protogranular peridotites, the porphyroclastic samples contain higher amounts of median to small-grained minerals (0.2–1.5 mm). Olivine and Opx porphyroclasts reach up to 2 mm in size, and are surrounded by smaller neoblasts (<1 mm) of other minerals, including Cpx and spinel. Lherzolites dominate the xenolith population (16 of 20), have relatively high Opx modes (21%–28%; Table 1) and contain interstitial spinel and “clear” Cpx with rare spongy rims (Fig. S1D). Exsolution lamellae are occasionally present in some large Opx or Cpx grains. The four harzburgites have distinctly lower modal Opx (13%–16%) and three contain cloudy Cpx intergrown with spinel (Fig. S1F), whereas the fourth harzburgite (17DSH-20) has relatively “clear” Cpx and isolated interstitial spinel similar to the lherzolites. No melt/fluid inclusions were observed in cloudy Cpx. Tiny (generally less than 5 μm), unevenly distributed spinel/chromite inclusions occur in cloudy Cpx in addition to large intergrown spinel grains (Fig. S2).

SUPPLEMENTARY INFORMATION 3. ANALYTICAL METHODS

Major-element compositions of whole rocks (WR) were measured at the State Key Laboratory of Geological Processes and Mineral Resources (GPMR), China University of Geosciences (CUG), Wuhan. Analyses were conducted by X-ray fluorescence (XRF) on fused glass disks using a Shimadzu XRF-1800 instrument. The detailed analytical routines are described by Lin et al. (2019). The analytical accuracy is within 3% for most elements, except Cr_2O_3 (3.3%), based on reference material GBW07102 (ultramafic) and GBW07105 (basalt) (Table S1).

In-situ major-element compositions of minerals (Table S2) were determined by a JEOL JXA-8100 Electron Probe Micro Analyzer (EPMA), equipped with four wavelength-dispersive spectrometers (WDS), using an accelerating voltage of 15 kV and a sample current of 20 nA at CUG Wuhan. The nominal diameter of the electron beam was 1 μm . Data were corrected online using a modified ZAF (atomic number, absorption, fluorescence) correction procedure. The following standards were used for quantification: Jadeite (Na), Rutile (Ti), Pyrope Garnet (Al, Fe, Mg and Si), Rhodonite (Mn), Diopside (Ca), Sanidine (K) and Nickel (Ni).

In-situ trace-element analyses of Cpx were conducted using laser ablation-inductively-coupled plasma-mass spectrometry (LA-ICP-MS), employing a GeoLas 2005 coupled to an Agilent 7500a instrument, with an ablation spot size of 44 μm at CUG Wuhan. Each analysis included ~20–30s of background acquisition (from a gas blank) followed by 50s of data acquisition for the sample. NIST SRM 610 was used to correct the time-dependent drift of sensitivity and mass discrimination. The USGS reference glasses (BCR-2G, BHVO-2G and BIR-1G) were measured as unknowns. The element contents of samples were determined using the USGS reference glasses for external calibration, without applying internal standardization, and normalization of the sum of all metal major oxides to 100 wt% was applied (Liu et al., 2008). Results for reference materials are given in Table S3, with most element concentrations except Ni (up to 16%) and Zn (up to 14%) agreeing within 10% or better with accepted values.

In-situ high-precision trace-element analyses of Cpx from twelve selected samples were conducted with a Thermo Finnigan ElementXR ICP-MS linked to an M-50 HR laser system (Resonetics) in the Institute of Geosciences at Goethe-Universität Frankfurt (GUF), following the approach detailed in Aulbach et al. (2017). The laser ablation instrument is equipped with a low-wavelength laser ($\lambda = 193 \text{ nm}$) and a dual volume sample cell. Analytical conditions included a laser spot size of 40 μm for Cpx, a repetition rate of 9 Hz and energy of 80 mJ with a 50% attenuator at low resolution (LR). NIST 612 was used as a calibration standard, and BIR-1G was measured as an unknown to monitor performance. Average silica contents as determined by EPMA were used for internal standardization and data were reduced with the Glitter software (Griffin et al., 2008). Concentrations of most trace elements in BIR-1G agree within 20% of accepted values in the LR mode (Table S3), except for U (21%).

In-situ Sr isotopic compositions of Cpx were performed at CUG Wuhan on a Thermo Fisher Scientific Neptune plus MC-ICP-MS coupled with a 193 nm laser ablation system (Geolas 2005) using a spot size of 120 μm . Each analysis consists of ca. 30 s background acquisition (gas blank) followed by 50 s of data acquisition (laser ablation) from the sample. The Faraday collector configuration was composed of an array from L4 to H3, used to monitor isotopes of Kr, Rb, Er, Yb and Sr (detailed experimental conditions in Tong et al., 2016). Analytical results for reference materials measured as unknowns (BHVO-2G: $^{87}\text{Sr}/^{86}\text{Sr} = 0.70352 \pm 0.00011$ 2SE, $n = 26$; HNB08: $^{87}\text{Sr}/^{86}\text{Sr} = 0.70381 \pm 0.00033$ 2SE, $n = 6$) agree with recommended values within analytical uncertainty ($^{87}\text{Sr}/^{86}\text{Sr} = 0.703469 \pm 0.000014$ 2SE and 0.703765 ± 0.000004 2SE, respectively; Tong et al., 2016).

Additionally, a RESOLUTION (Resonetics) 193nm ArF Excimer Laser (CompexPro 102, Coherent) was linked to a Thermo-Finnigan Neptune multi-collector (MC) ICPMS to measure Sr isotopes at GUF, using Faraday Cups in static collection mode and following the procedural details in Aulbach et al. (2016). Analyses lasted 45 s and were run at spot sizes of 120 μm (cloudy Cpx) or 160 μm , employing a 10 Hz repetition rate. Analysis of an in-house standard during the sequence, isotopically homogeneous plagioclase MIR-1, yielded $^{87}\text{Sr}/^{86}\text{Sr}$ (0.703138 ± 0.000017 1σ , $n = 2$) indistinguishable from the TIMS-derived value $^{87}\text{Sr}/^{86}\text{Sr}$ (0.703096 ± 0.000050 ; Rankenburg, 2002), while BCR-2 and BHVO-2 measured as unknowns yielded 0.705033 ± 0.000061 ($n = 2$) and 0.703485 ± 0.000006 , comparing well with GeoREM preferred values of 0.705003 ± 0.00004 and 0.703469 ± 0.000007 , respectively (<http://georem.mpch-mainz.gwdg.de>). As $^{87}\text{Rb}/^{86}\text{Sr}$ in peridotitic Cpx measured here is much lower (<0.026) than in the basalt glass BHVO-2 (0.50), the results after correction for the isobaric interference of ^{87}Rb on ^{87}Sr are considered reliable. Median measurement uncertainties of ± 0.00013 (2SE) suggest

that samples are homogeneous at the grain scale, while median 1σ of 0.00009 for analyses of multiple grains and multiple spots per grain indicate homogeneity at the sample scale.

Whole-rock highly siderophile element (HSE) abundances and Re-Os isotope analyses were conducted at CUG Beijing, using an isotope dilution technique coupled with Carius tube aqua regia digestion described by Li et al. (2014) and Xu et al. (2020). Osmium abundances and isotopic ratios were determined by negative thermal ionization mass spectrometry (N-TIMS) using a Thermo Scientific Triton Plus, and the measurement procedures and cup configuration are similar to those of Xu et al. (2020), which are modified from Liu and Pearson (2014). The measured Os isotopic ratios were corrected for mass-dependent fractionation using $^{192}\text{Os}/^{188}\text{Os} = 3.08271$ via the exponential law and oxygen isotope interferences using $^{17}\text{O}/^{16}\text{O} = 0.0003749$ and $^{18}\text{O}/^{16}\text{O} = 0.0020439$ (Nier, 1950). In the analysis routine, 1 ng loads of the Durham Romil Osmium Standard (DROsS) and of the University of Maryland Johnson Matthey Osmium Standard (UMd) were repeatedly measured, yielding $^{187}\text{Os}/^{188}\text{Os}$ ratios of 0.160927 ± 0.000054 (2σ , $n = 10$) and 0.113796 ± 0.000022 (2σ , $n = 10$), respectively, which are in agreement with the accepted values (0.160924 ± 0.000004 for DROsS and 0.113787 ± 0.000008 for UMD; Luguet et al., 2008). Reference material UB-N was analyzed as an unknown, yielding Os concentration of 3.71 ng and $^{187}\text{Os}/^{188}\text{Os}$ ratio of 0.12742 ± 0.00007 (2SE, Xu et al., 2020) consistent with the recommended values within uncertainties (3.97 ± 0.38 and 0.12732 ± 0.00085 , respectively; Ishikawa et al., 2014). The abundances of other HSE were measured by sector-field (SF) ICP-MS using a Thermo Scientific Element XR. A mixed standard solution of Ir, Ru, Pt, Pd and Re (roughly mantle-like HSE abundances) were measured per five sample analyses to monitor instrumental mass bias. The measured HSE concentrations of UB-N were 3.34 ppb for Ir, 6.97 ppb for Ru, 7.44 ppb for Pt, 5.93 ppb for Pd, 0.21 ppb for Re, respectively (Xu et al., 2020), which are also consistent with in literature data (3.41 ± 0.26 , 6.80 ± 0.47 , 6.98 ± 0.35 , 5.55 ± 0.17 and 0.210 ± 0.018 , respectively, Ishikawa et al., 2014). Total procedural blank levels during this analytical campaign were 3.51 pg for Os, 0.03 pg for Ir, 0.86 pg for Ru, 2.95 pg for Pt, 22.76 pg for Pd, and 0.44 pg for Re, which result in insignificant corrections of all elements both in the reference material and in samples measured in this study (<1%).

REFERENCES CITED

- Aulbach, S., Gerdes, A., and Viljoen, K.S., 2016, Formation of diamondiferous kyanite–eclogite in a subduction mélange: *Geochimica et Cosmochimica Acta*, v. 179, p. 156–176, <https://doi.org/10.1016/j.gca.2016.01.038>.
- Aulbach, S., Sun, J., Tappe, S., Höfer, H.E., and Gerdes, A., 2017, Volatile-rich metasomatism in the Cratonic Mantle beneath SW Greenland: link to Kimberlites and Mid-lithospheric discontinuities: *Journal of Petrology*, v. 58, p. 2311–2338, <https://doi.org/10.1093/petrology/egy009>.
- Dasgupta, R., Hirschmann, M.M., McDonough, W.F., Spiegelman, M., and Withers, A.C., 2009, Trace element partitioning between garnet lherzolite and carbonatite at 6.6 and 8.6 GPa with applications to the geochemistry of the mantle and of mantle-derived melts: *Chemical Geology*, v. 262, p. 57–77, <https://doi.org/10.1016/j.chemgeo.2009.02.004>.
- Green, T.H., Blundy, J.D., Adam, J., and Yaxley, G.M., 2000, SIMS determination of trace element partition coefficients between garnet, clinopyroxene and hydrous basaltic liquids at 2–7.5 GPa and 1080–1200°C: *Lithos*, v. 53, p. 165–187, [https://doi.org/10.1016/S0024-4937\(00\)00023-2](https://doi.org/10.1016/S0024-4937(00)00023-2).

- Griffin, W.L., Powell, W.J., Pearson, N.J., and O'Reilly, S.Y., 2008, GLITTER: Data reduction software for laser ablation ICP-MS, *in* Sylvester, P.J., ed., *Laser Ablation ICP-MS in the Earth Sciences: Current Practices and Outstanding Issues*. Mineralogical Association of Canada, Short Course Series 40, p. 308–311.
- Guo, P., Ionov, D.A., Xu, W.L., Wang, C.G., and Luan, J.P., 2020, Mantle and recycled oceanic crustal components in mantle xenoliths from northeastern China and their mantle sources: *Journal of Geophysical Research. Solid Earth*, v. 125, <https://doi.org/10.1029/2019JB018232>.
- Guo, Z., Chen, Y.J., Ning, J., Yang, Y., Afonso, J.C., and Tang, Y., 2016, Seismic evidence of on-going sublithosphere upper mantle convection for intra-plate volcanism in Northeast China: *Earth and Planetary Science Letters*, v. 433, p. 31–43, <https://doi.org/10.1016/j.epsl.2015.09.035>.
- Guo, Z., Wang, K., Yang, Y., Tang, Y., John Chen, Y., and Hung, S.H., 2018, The origin and mantle dynamics of quaternary intraplate volcanism in Northeast China from joint inversion of surface wave and body wave: *Journal of Geophysical Research. Solid Earth*, v. 123, p. 2410–2425, <https://doi.org/10.1002/2017JB014948>.
- Hao, Y.T., Xia, Q.K., Jia, Z.B., Zhao, Q.C., Li, P., Feng, M., and Liu, S.C., 2016, Regional heterogeneity in the water content of the Cenozoic lithospheric mantle of Eastern China: *Journal of Geophysical Research. Solid Earth*, v. 121, p. 517–537, <https://doi.org/10.1002/2015JB012105>.
- Ishikawa, A., Senda, R., Suzuki, K., Dale, C.W., and Meisel, T., 2014, Re-evaluating digestion methods for highly siderophile element and ¹⁸⁷Os isotope analysis: Evidence from geological reference materials: *Chemical Geology*, v. 384, p. 27–46, <https://doi.org/10.1016/j.chemgeo.2014.06.013>.
- Jahn, B.M., Wu, F.Y., and Chen, B., 2000, Massive granitoids generation in Central Asia: Nd isotope evidence and implication for continental growth in the Phanerozoic: *Episodes*, v. 23, p. 82–92, <https://doi.org/10.18814/epiiugs/2000/v23i2/001>.
- Klemme, S., Van der Laan, S.R., Foley, S.F., and Günther, D., 1995, Experimentally determined trace and minor element partitioning between clinopyroxene and carbonatite melt under upper mantle conditions: *Earth and Planetary Science Letters*, v. 133, p. 439–448, [https://doi.org/10.1016/0012-821X\(95\)00098-W](https://doi.org/10.1016/0012-821X(95)00098-W).
- Lei, J., and Zhao, D., 2005, P-wave tomography and origin of the Changbai intraplate volcano in Northeast Asia: *Tectonophysics*, v. 397, p. 281–295, <https://doi.org/10.1016/j.tecto.2004.12.009>.
- Li, J., Jiang, X.Y., Xu, J.F., Zhong, L.F., Wang, X.C., Wang, G.Q., and Zhao, P.P., 2014, Determination of Platinum-Group Elements and Re-Os Isotopes using ID-ICP-MS and N-TIMS from a Single Digestion after Two-Stage Column Separation: *Geostandards and Geoanalytical Research*, v. 38, p. 37–50, <https://doi.org/10.1111/j.1751-908X.2013.00242.x>.
- Li, J.Y., 2006, Permian geodynamic setting of Northeast China and adjacent regions: closure of the Paleo-Asian Ocean and subduction of the Paleo-Pacific plate: *Journal of Asian Earth Sciences*, v. 26, p. 207–224, <https://doi.org/10.1016/j.jseaes.2005.09.001>.
- Lin, A.B., Zheng, J.P., Xiong, Q., Aulbach, S., Lu, J.G., Pan, S.K., Dai, H.K., and Zhang, H., 2019, A refined model for lithosphere evolution beneath the decratonized northeastern North China Craton: *Contributions to Mineralogy and Petrology*, v. 174, 15, <https://doi.org/10.1007/s00410-019-1551-0>.

- Liu, C., Zhu, G., Xie, C., Zhang, S., Li, Y., Su, N., and Xiao, S., 2019, Location and sinistral displacement of the eastern Liaoyuan Accretionary Belt along the Tan–Lu Fault Zone, NE China: *Journal of Asian Earth Sciences*, v. 172, p. 409–422, <https://doi.org/10.1016/j.jseaes.2018.10.002>.
- Liu, J., and Pearson, D.G., 2014, Rapid, precise and accurate Os isotope ratio measurements of nanogram to sub-nanogram amounts using multiple Faraday collectors and amplifiers equipped with $10^{12} \Omega$ resistors by N-TIMS: *Chemical Geology*, v. 363, p. 301–311, <https://doi.org/10.1016/j.chemgeo.2013.11.008>.
- Liu, J., Han, J., and Fyfe, W.S., 2001, Cenozoic episodic volcanism and continental rifting in northeast China and possible link to Japan Sea development as revealed from K–Ar geochronology: *Tectonophysics*, v. 339, p. 385–401, [https://doi.org/10.1016/S0040-1951\(01\)00132-9](https://doi.org/10.1016/S0040-1951(01)00132-9).
- Liu, Y.S., Hu, Z.C., Gao, S., Guenther, D., Xu, J., Gao, C.G., and Chen, H.H., 2008, In situ analysis of major and trace elements of anhydrous minerals by LA-ICP-MS without applying an internal standard: *Chemical Geology*, v. 257, p. 34–43, <https://doi.org/10.1016/j.chemgeo.2008.08.004>.
- Luguet, A., Nowell, G.M., and Pearson, D.G., 2008, $^{184}\text{Os}/^{188}\text{Os}$ and $^{186}\text{Os}/^{188}\text{Os}$ measurements by Negative Thermal Ionisation Mass Spectrometry (N-TIMS): Effects of interfering element and mass fractionation corrections on data accuracy and precision: *Chemical Geology*, v. 248, p. 342–362, <https://doi.org/10.1016/j.chemgeo.2007.10.013>.
- McDonough, W.F., and Sun, S.S., 1995, The composition of the Earth: *Chemical Geology*, v. 120, p. 223–253, [https://doi.org/10.1016/0009-2541\(94\)00140-4](https://doi.org/10.1016/0009-2541(94)00140-4).
- Nier, A.O., 1950, A redetermination of the relative abundances of the isotopes of carbon, nitrogen, oxygen, argon, and potassium: *Physical Review*, v. 77, p. 789–793, <https://doi.org/10.1103/PhysRev.77.789>.
- Pan, S.K., Zheng, J.P., Chu, L.L., and Griffin, W.L., 2013, Coexistence of the moderately refractory and fertile mantle beneath the eastern Central Asian Orogenic Belt: *Gondwana Research*, v. 23, p. 176–189, <https://doi.org/10.1016/j.gr.2012.03.001>.
- Pan, S.K., Zheng, J.P., Griffin, W.L., Xu, Y.X., and Li, X.Y., 2015, Nature and evolution of the lithospheric mantle beneath the eastern Central Asian Orogenic Belt: Constraints from peridotite xenoliths in the central part of the Great Xing’an Range, NE China: *Lithos*, v. 238, p. 52–63, <https://doi.org/10.1016/j.lithos.2015.09.013>.
- Rankenburg, K., 2002, Megacrysts in volcanic rocks of the Cameroon volcanic line: constraints on magma genesis and contamination. [Ph.D. thesis]: Frankfurt am Main, Institut für Mineralogie, Goethe-Universität, 82 p.
- Tang, Y., Obayashi, M., Niu, F., Grand, S.P., Chen, Y.J., Kawakatsu, H., Tanaka, S., Ning, J., and Ni, J.F., 2014, Changbaishan volcanism in northeast China linked to subduction-induced mantle upwelling: *Nature Geoscience*, v. 7, p. 470–475, <https://doi.org/10.1038/ngeo2166>.
- Tong, X.R., Liu, Y.S., Hu, Z.C., Chen, H.H., Zhou, L., Hu, Q.H., Xu, R., Deng, L.X., Chen, C.F., Yang, L., and Gao, S., 2016, Accurate determination of Sr isotopic compositions in clinopyroxene and silicate glasses by LA-MC-ICP-MS: *Geostandards and Geoanalytical Research*, v. 40, p. 85–99, <https://doi.org/10.1111/j.1751-908X.2015.00315.x>.
- Wang, L.C., 1996, Occurrence of the Dashihe olivine deposit in Jilin province, China [in Chinese with English abstract]: *Journal of Changchun University of Earth Sciences*, v. 26, p. 43–46.

- Wu, F.Y., Walker, R.J., Ren, X.W., Sun, D.Y., and Zhou, X.H., 2003, Osmium isotopic constraints on the age of lithospheric mantle beneath northeastern China: *Chemical Geology*, v. 196, p. 107–129, [https://doi.org/10.1016/S0009-2541\(02\)00409-6](https://doi.org/10.1016/S0009-2541(02)00409-6).
- Xu, W.L., Pei, F.P., Wang, F., Meng, E., Ji, W.Q., Yang, D.B., and Wang, W., 2013, Spatial–temporal relationships of Mesozoic volcanic rocks in NE China: constraints on tectonic overprinting and transformations between multiple tectonic regimes: *Journal of Asian Earth Sciences*, v. 74, p. 167–193, <https://doi.org/10.1016/j.jseaes.2013.04.003>.
- Xu, Y., Liu, J., Xiong, Q., Su, B.X., Scott, J.M., Xu, B., Zhu, D.C., and Pearson, D.G., 2020, The complex life cycle of oceanic lithosphere: A study of Yarlung-Zangbo ophiolitic peridotites, Tibet: *Geochimica et Cosmochimica Acta*, v. 277, p. 175–191, <https://doi.org/10.1016/j.gca.2020.03.024>.
- Xu, Y.G., Menzies, M.A., Thirlwall, M.F., Huang, X.L., Liu, Y., and Chen, X.M., 2003, “Reactive” harzburgites from Huinan, NE China: products of the lithosphere–asthenosphere interaction during lithospheric thinning?: *Geochimica et Cosmochimica Acta*, v. 67, p. 487–505, [https://doi.org/10.1016/S0016-7037\(02\)01089-X](https://doi.org/10.1016/S0016-7037(02)01089-X).
- Yan, J., and Zhao, J.X., 2008, Cenozoic alkali basalts from Jingpohu, NE China: the role of lithosphere–asthenosphere interaction: *Journal of Asian Earth Sciences*, v. 33, p. 106–121, <https://doi.org/10.1016/j.jseaes.2007.11.001>.
- Ying, J., Zhou, X., and Zhang, H., 2004, Geochemical and isotopic investigation of the Laiwu–Zibo carbonatites from western Shandong Province, China, and implications for their petrogenesis and enriched mantle source: *Lithos*, v. 75, p. 413–426, <https://doi.org/10.1016/j.lithos.2004.04.037>.
- Yu, S.Y., Xu, Y.G., Huang, X.L., Ma, J.L., Ge, W.C., Zhang, H.H., and Qin, X.F., 2009, Hf–Nd isotopic decoupling in continental mantle lithosphere beneath Northeast China: effects of pervasive mantle metasomatism: *Journal of Asian Earth Sciences*, v. 35, p. 554–570, <https://doi.org/10.1016/j.jseaes.2009.04.005>.
- Yu, S.Y., Xu, Y.G., Ma, J.L., Zheng, Y.F., Kuang, Y.S., Hong, L.B., Ge, W.C., and Tong, L.X., 2010, Remnants of oceanic lower crust in the subcontinental lithospheric mantle: trace element and Sr–Nd–O isotope evidence from aluminous garnet pyroxenite xenoliths from Jiaohe, Northeast China: *Earth and Planetary Science Letters*, v. 297, p. 413–422, <https://doi.org/10.1016/j.epsl.2010.06.043>.
- Zhang, M., Yang, J.H., Sun, J.F., Wu, F.Y., and Zhang, M., 2012, Juvenile subcontinental lithospheric mantle beneath the eastern part of the Central Asian Orogenic Belt: *Chemical Geology*, v. 328, p. 109–122, <https://doi.org/10.1016/j.chemgeo.2012.07.010>.
- Zhang, Y.L., Ge, W.C., Sun, J., Yang, H., Liu, Z.C., and Liu, J., 2019, Age and composition of the subcontinental lithospheric mantle beneath the Xing’an–Mongolia Orogenic Belt: Implications for the construction of microcontinents during accretionary orogenesis: *Lithos*, v. 326–327, p. 556–571, <https://doi.org/10.1016/j.lithos.2019.01.013>.
- Zhang, Y.L., Liu, C.Z., Ge, W.C., Wu, F.Y., and Chu, Z.Y., 2011, Ancient sub-continental lithospheric mantle (SCLM) beneath the eastern part of the Central Asian Orogenic Belt (CAOB): Implications for crust–mantle decoupling: *Lithos*, v. 126, p. 233–247, <https://doi.org/10.1016/j.lithos.2011.07.022>.
- Zhou, Q., Wu, F.Y., Chu, Z.Y., Yang, Y.H., Sun, D.Y., and Ge, W.C., 2007, Sr–Nd–Hf–Os isotopic characterizations of the Jiaohe peridotite xenoliths in Jilin province and constraints on the lithospheric mantle age in northeastern China [in Chinese with English abstract]: *Acta Petrologica Sinica (Yanshi Xuebao)*, v. 23, p. 1269–1280.

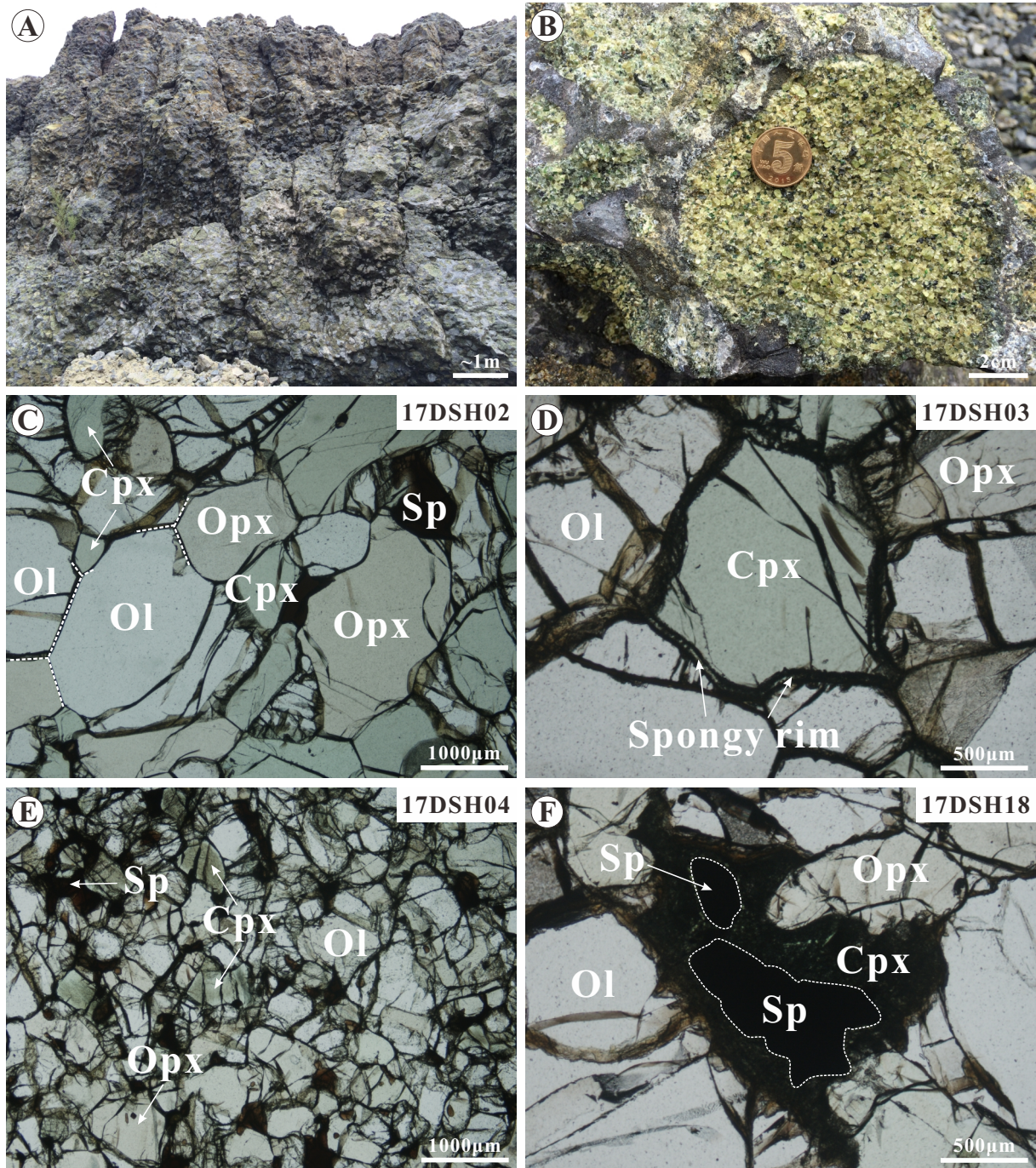


Figure S1. Field photographs (A–B) of Jiaohe mantle xenolith locality and photomicrographs (C–F) of spinel peridotite xenoliths from Jiaohe in transmitted plane-polarized light (PPL). (C) Lherzolite 17DSH02 with coarse-grained protogranular texture showing typical triple junctions among mineral grains (highlighted with white stipples). (D) Spongy rim on Cpx in lherzolite 17DSH03 appearing opaque in PPL. (E) “Porphyroclastic” texture in fine-grained lherzolite 17DSH04. (F) Spinel with curved grain boundary (highlighted with white stipples) intergrown with cloudy Cpx in harzburgite 17DSH18. Ol, olivine; Opx, orthopyroxene; Cpx, clinopyroxene; Sp, spinel.

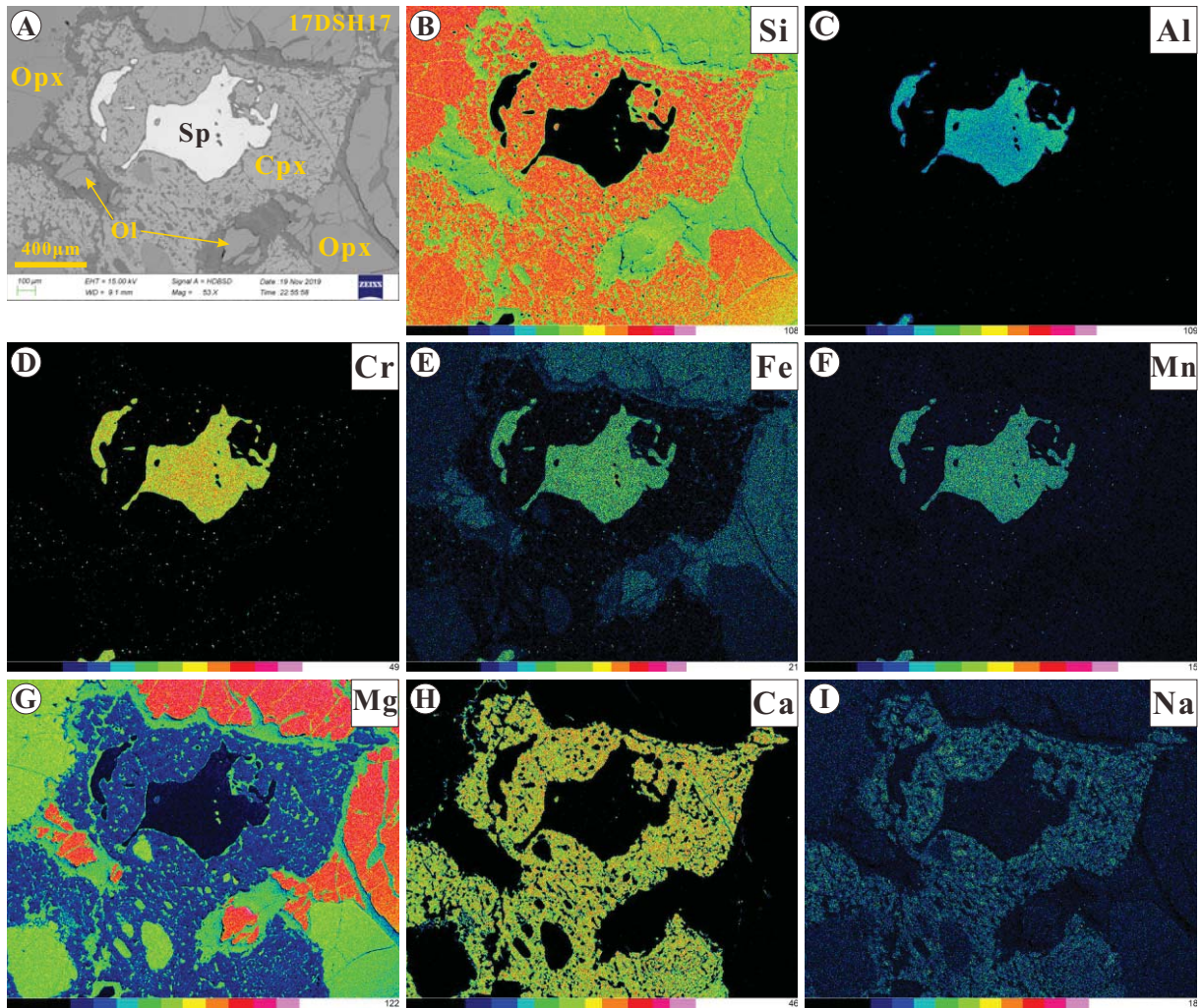


Figure S2. Backscattered electron (BSE) image and eight elemental maps of cloudy clinopyroxene from the Jiaohe harzburgites. Color bar at the bottom indicates the relative contents of the selected elements.

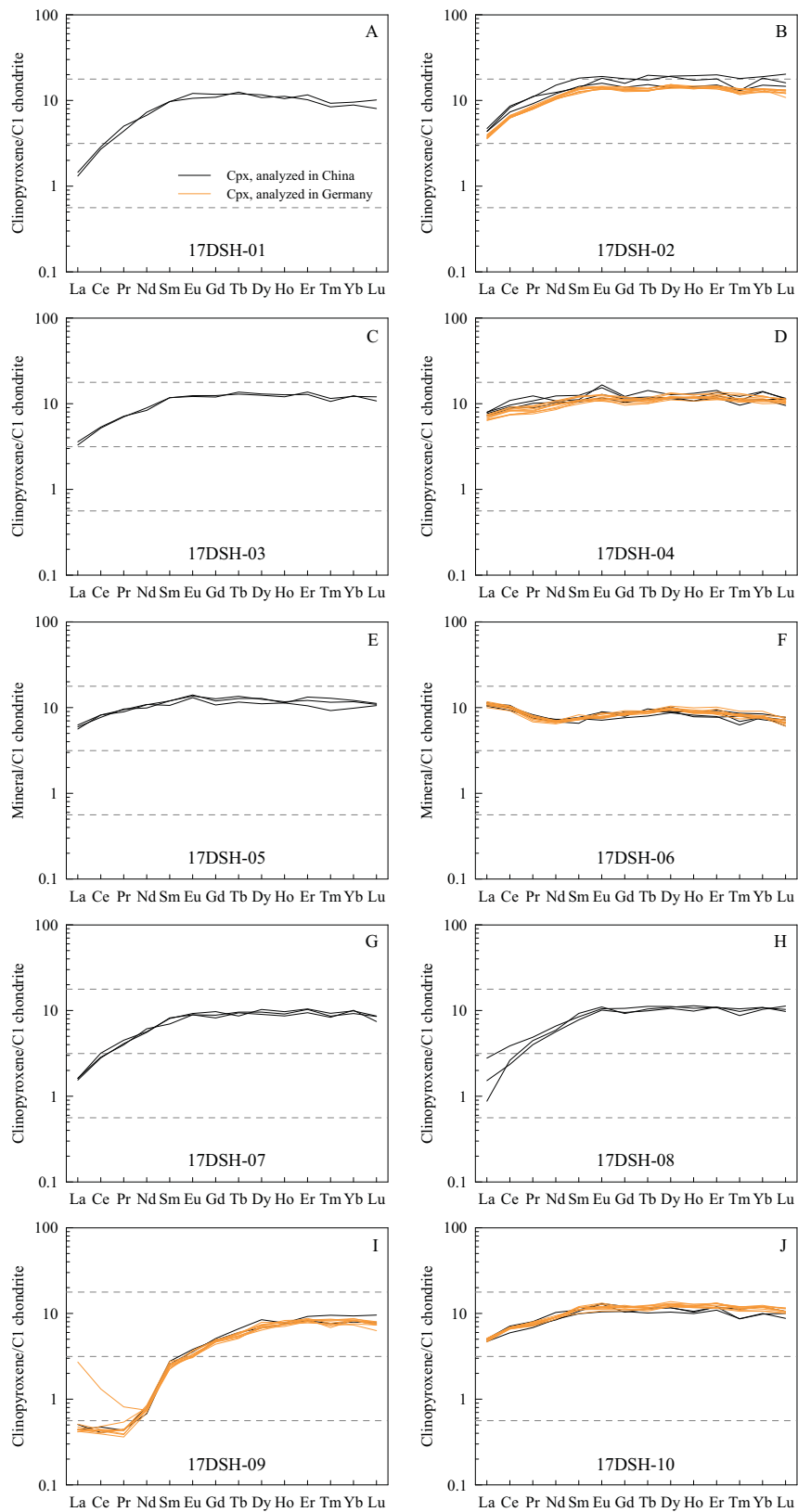


Figure S3. Chondrite-normalized REE patterns (A–T) and primitive mantle-normalized multi-element plots (U–AN) for all analyzed clinopyroxenes of the studied peridotite xenoliths. Chondrite and Primitive Mantle from [McDonough and Sun \(1995\)](#).

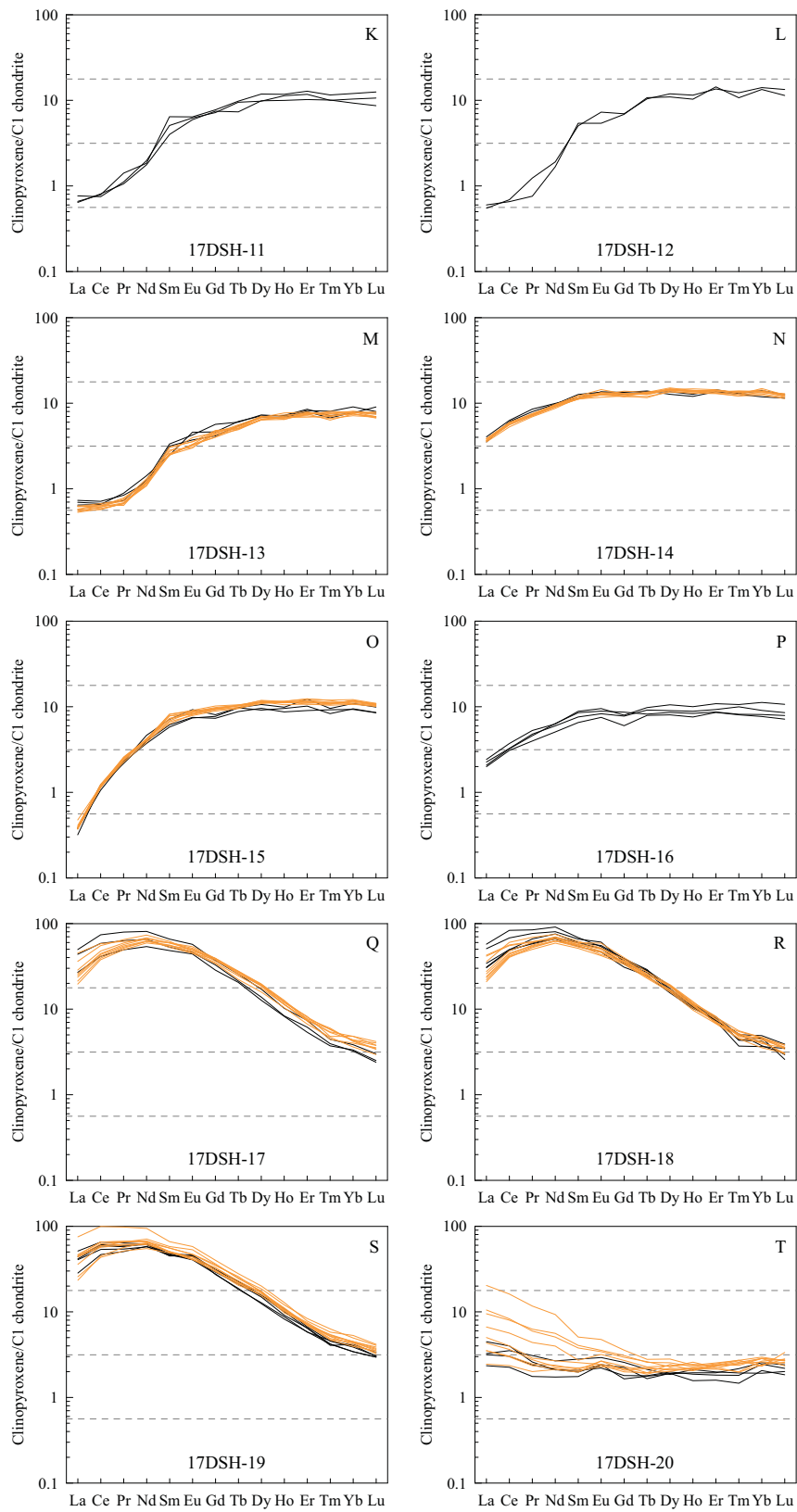


Figure S3. (Continued).

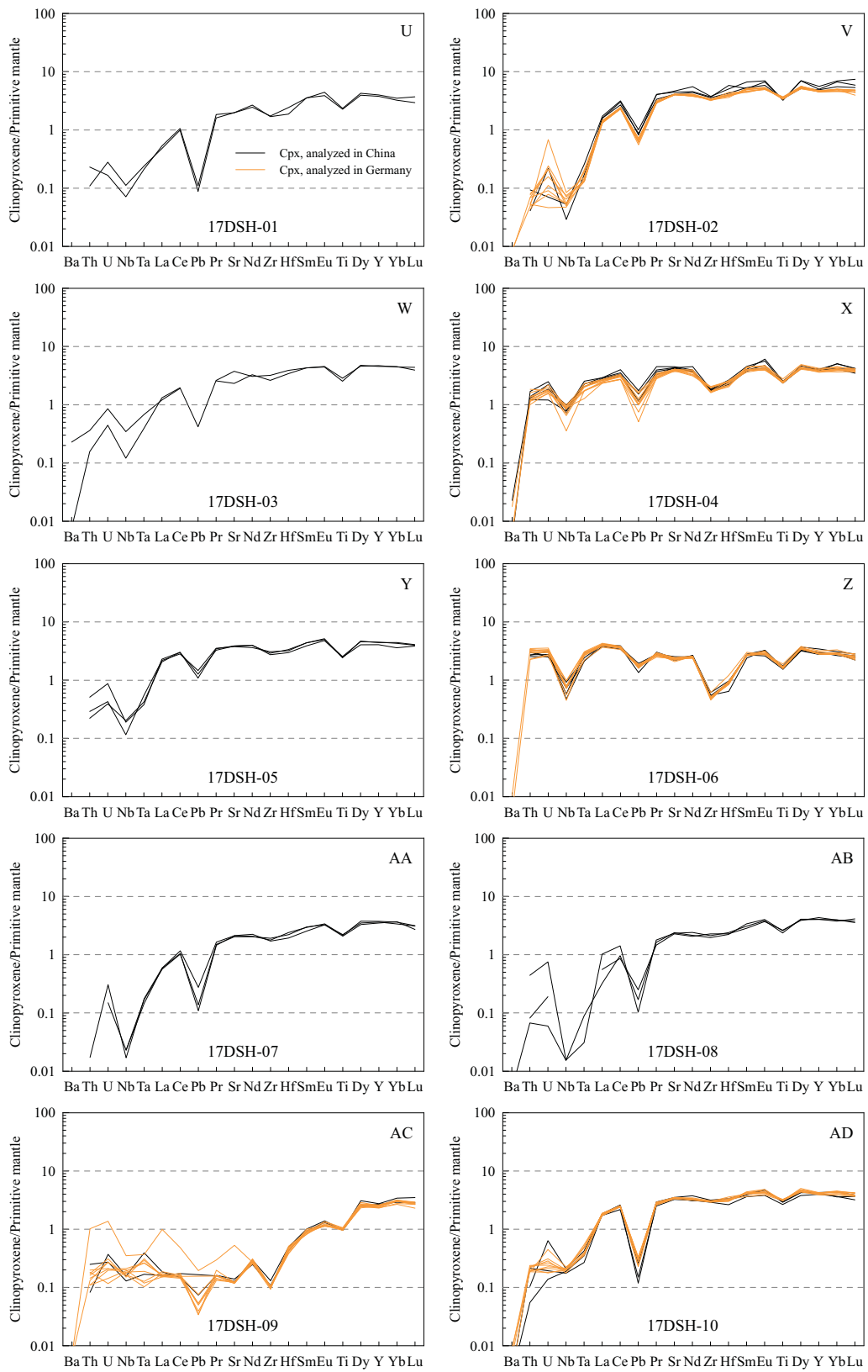


Figure S3. (Continued).

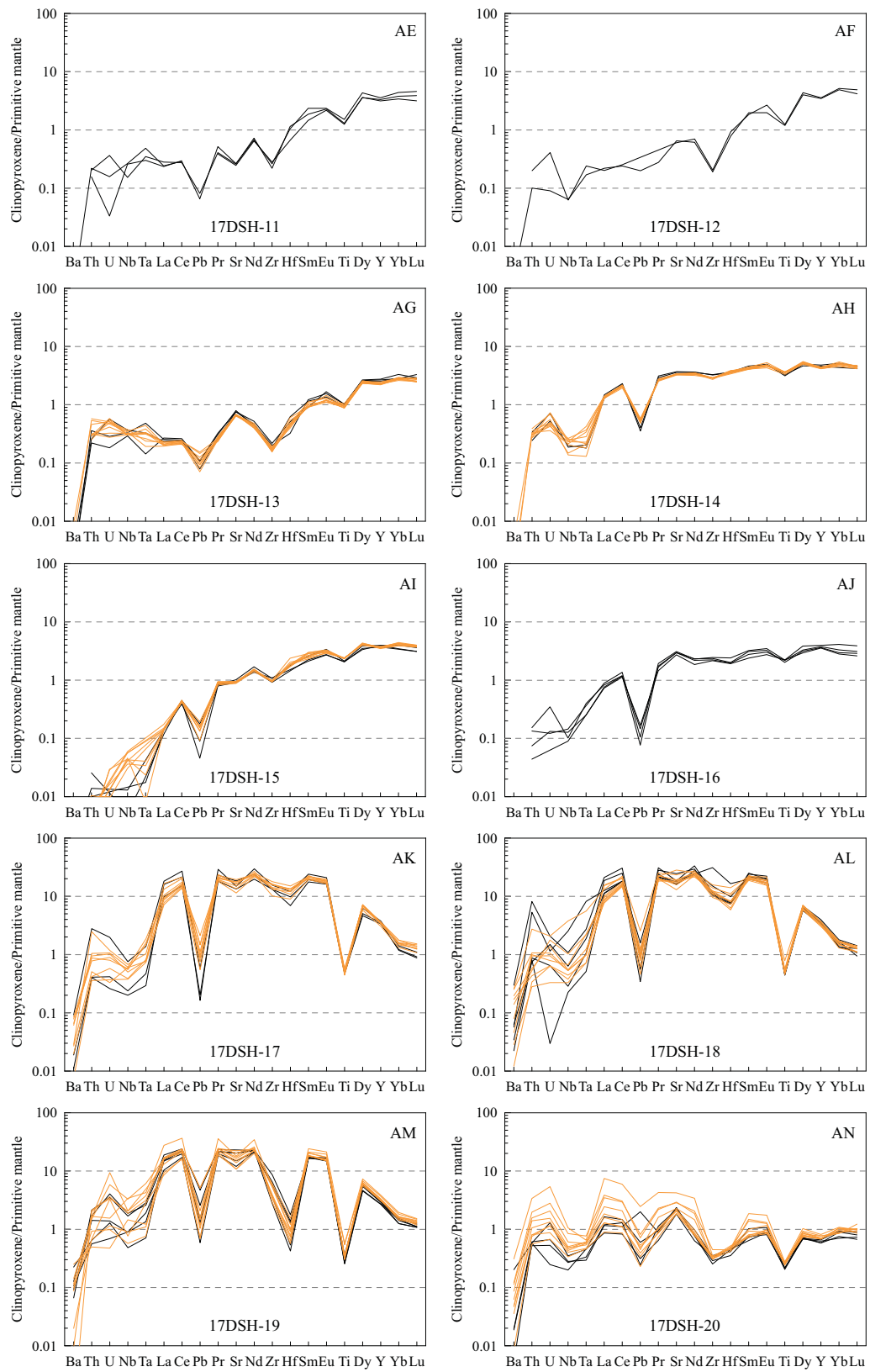


Figure S3. (Continued).

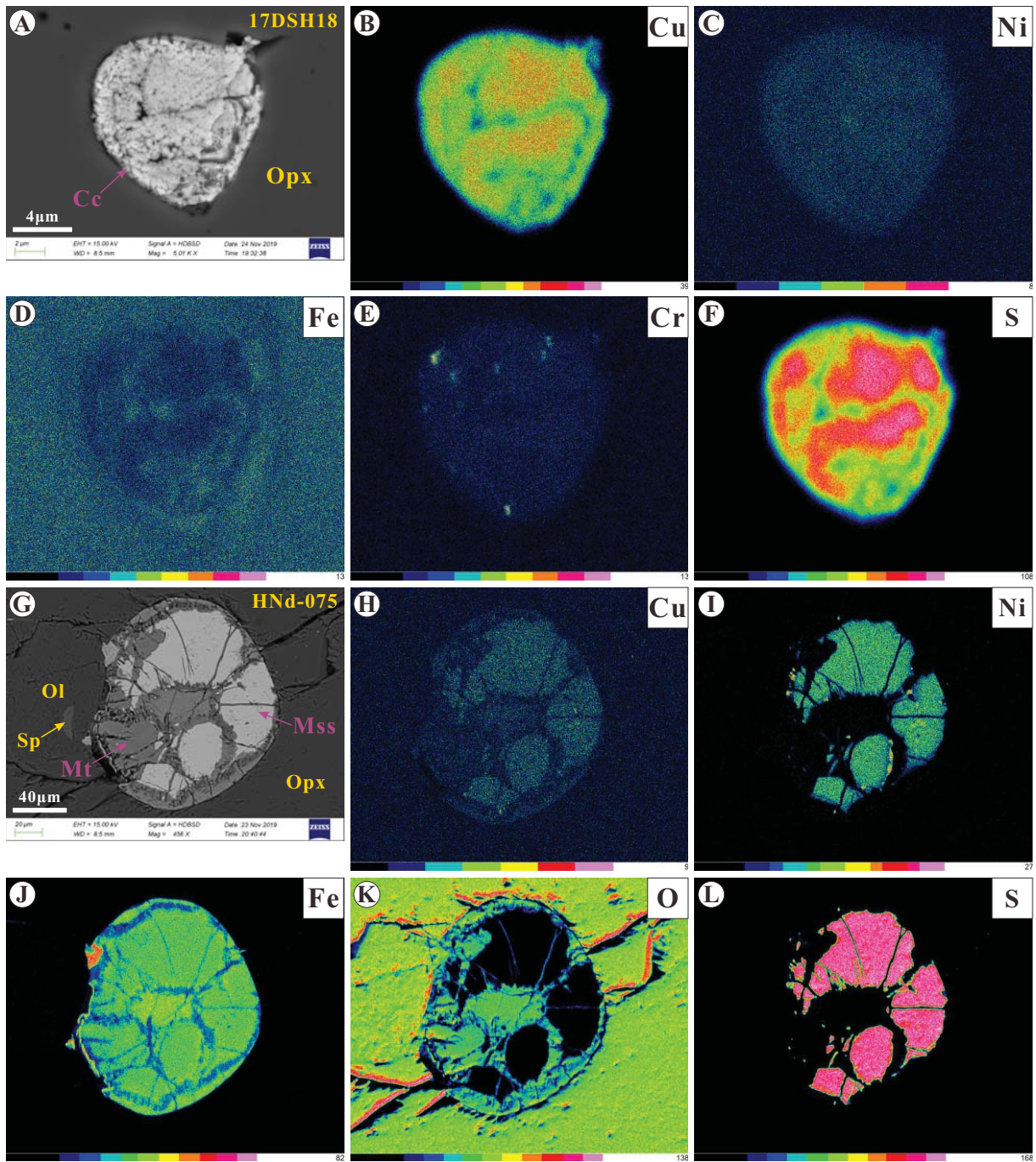


Figure S4. BSE images (2) and elemental maps (10) of sulfide grains from a Jiaohe harzburgite (A–F) and a Huinan peridotite (G–L). Color bar at the bottom indicates the relative contents of the selected elements.

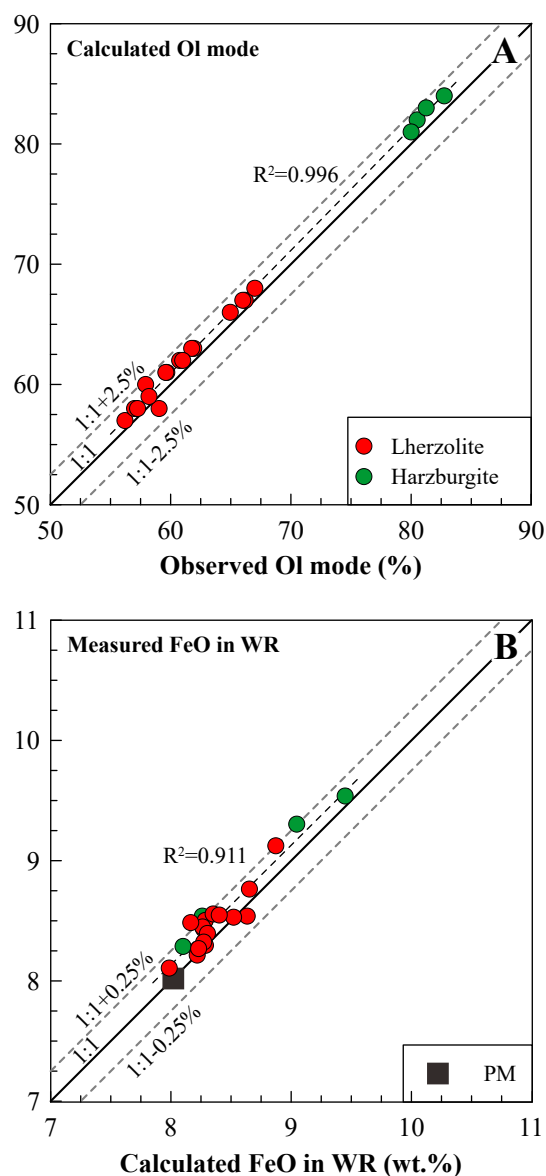


Figure S5. Plots of observed vs calculated olivine (Ol) mode (A) and calculated vs measured FeO in whole rocks (WR) (B) for Jiaohé peridotite xenoliths in this study. (A) Observed mineral modes were obtained by point counting (Table S6), whereas calculated mineral modes were calculated by least squares method from whole-rock and mineral analyses (Table 1). (B) FeO contents in WR were calculated using observed mineral modes and mineral analyses (Table S6), whereas measured FeO contents in WR were acquired by XRF (Table S1). Solid lines (1:1) show equal contents for these samples, dashed lines mark difference of $\pm 2.5\%$ in (A) and $\pm 0.25\%$ in (B).

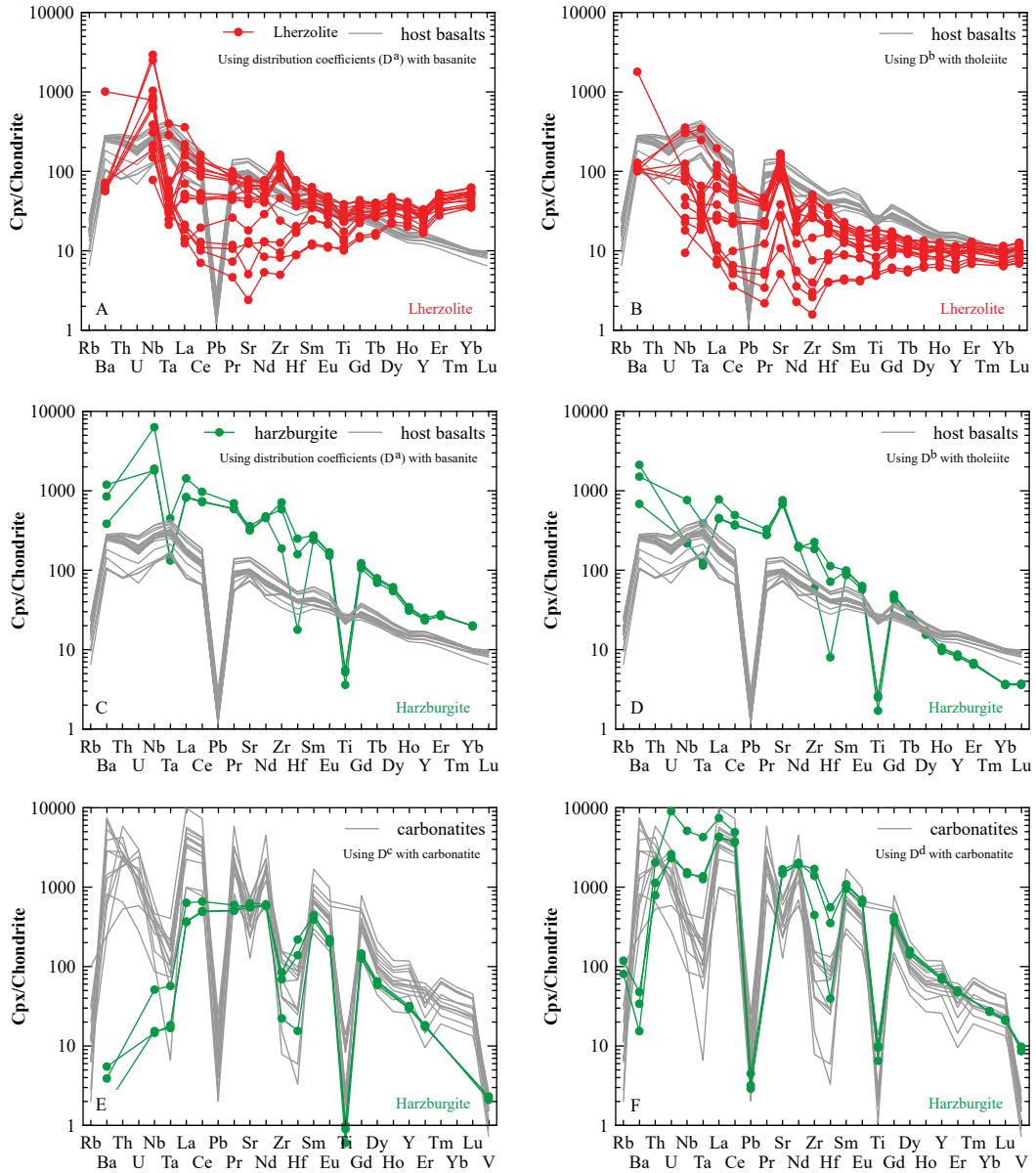


Figure S6. Calculated melts in equilibrium with Cpx, using distribution coefficients with basanite (Green et al., 2000), tholeiite (Green et al., 2000) and carbonatite (Klemme et al., 1995; Dasgupta et al., 2009), respectively, as listed in Table S7. Shown for comparison are the ranges of Jingpohu host basalts (Yan and Zhao, 2008) and carbonatites from western Shandong (Ying et al., 2004). Normalizing values are from McDonough and Sun (1995).